Unravelling Mangrove Storm Damage Resistance for Sustainable Flood Defense Safety Using 3D-Printed Mimics

van Hespen, Rosanna ; Gijón Mancheño, Alejandra; Kleinhans, Maarten; van Belzen, Jim; van Bijsterveldt, Celine E.J.; de Smit, Jaco; Hu, Zhan; Borsje, Bas W.; Hofland, Bas; Bouma, Tjeerd J.

DOI
10.3390/su17062602

Publication date
2025

Document Version
Final published version

Published in
Sustainability

Citation (APA)
van Hespen, R., Gijón Mancheño, A., Kleinhans, M., van Belzen, J., van Bijsterveldt, C. E. J., de Smit, J., Hu, Z., Borsje, B. W., Hofland, B., & Bouma, T. J. (2025). Unravelling Mangrove Storm Damage Resistance for Sustainable Flood Defense Safety Using 3D-Printed Mimics. *Sustainability*, *17*(6), Article 2602. https://doi.org/10.3390/su17062602

sustainability

MDPI

Article

Unravelling Mangrove Storm Damage Resistance for Sustainable Flood Defense Safety Using 3D-Printed Mimics

Rosanna van Hespen [1,2,3,†], Alejandra Gijón Mancheño [4,*,†], Maarten Kleinhans [2], Jim van Belzen [1], Celine E. J. van Bijsterveldt [1,2,5], Jaco de Smit [1,3], Zhan Hu [3,6,7,*], Bas W. Borsje [8], Bas Hofland [4] and Tjeerd J. Bouma [1,2]

1 Department of Estuarine and Delta Systems, NIOZ Royal Netherlands Institute for Sea Research, 4401 NT Yerseke, Zeeland, The Netherlands; jim.van.belzen@nioz.nl (J.v.B.); tjeerd.bouma@nioz.nl (T.J.B.)
2 Department of Physical Geography, Faculty of Geosciences, Utrecht University, 3584 CS Utrecht, Utrecht, The Netherlands
3 Southern Marine Science and Engineering Guangdong Laboratory (Zhuhai), School of Marine Science, Sun Yat-sen University, Zhuhai 519082, China
4 Department of Hydraulic Engineering, Faculty of Civil Engineering and Geosciences, Delft University of Technology, 2628 CN Delft, Zuid-Holland, The Netherlands; b.hofland@tudelft.nl
5 Aquatic Ecology and Water Quality Management (AEW), Wageningen University & Research, 6708 PB Wageningen, Gelderland, The Netherlands
6 Guangdong Provincial Key Laboratory of Marine Resources and Coastal Engineering, Guangzhou 510275, China
7 Pearl River Estuary Marine Ecosystem Research Station, Ministry of Education, Zhuhai 519082, China
8 Water Engineering and Management, University of Twente, 7522 NB Enschede, Overijssel, The Netherlands; b.w.borsje@utwente.nl
* Correspondence: a.gijonmancheno-1@tudelft.nl (A.G.M.); huzh9@mail.sysu.edu.cn (Z.H.)
† These authors contributed equally to this work.

Abstract: Mangrove forests are vital for flood reduction, yet their failure mechanisms during storms are poorly known, hampering their integration into engineered coastal protection. In this paper, we aimed to unravel the relationship between the resistance of mangrove trees to overturning and root distribution and the properties of the soil, while avoiding damage to natural mangrove forests. We therefore (i) tested the stability of 3D-printed tree mimics that imitate typical shallow mangrove root systems, mimicking both damaged and intact root systems, in sediments representing the soil properties of contrasting mangrove sites, and subsequently (ii) tested if the existing stability models for terrestrial trees are applicable for mangrove tree species, which have unique shallow root systems to survive waterlogged soils. Root systems of different complexities were modeled after *Avicennia alba*, *Avicennia germinans*, and *Rhizophora stylosa*, and printed at a 1:100 scale using material densities matching those of natural tree roots, to ensure the geometric scaling of overturning moments. The mimic stability increased with the soil shear strength and root plate surface area. The optimal root configuration for mimic stability depended on the sediment properties: spreading root systems performed better in softer sediments, while concentrating root biomass near the trunk improved stability in stronger sediments. An adapted terrestrial tree resistance model reproduced our measurements well, suggesting that such models could be adapted to predict the stability of shallow-rooted mangroves living in waterlogged soils. Field tree-pulling experiments are needed to further confirm our conclusions with real-world data, examine complicating factors like root intertwining, and consider mangrove tree properties like aerial roots. Overall, this work establishes a foundation for incorporating mangrove storm damage into hybrid coastal protection systems.

check for updates

Received: 27 January 2025
Revised: 25 February 2025
Accepted: 13 March 2025
Published: 15 March 2025

Citation: van Hespen, R.; Gijón Mancheño, A.; Kleinhans, M.; van Belzen, J.; van Bijsterveldt, C.E.J.; de Smit, J.; Hu, Z.; Borsje, B.W.; Hofland, B.; Bouma, T.J. Unravelling Mangrove Storm Damage Resistance for Sustainable Flood Defense Safety Using 3D-Printed Mimics. *Sustainability* **2025**, *17*, 2602. https://doi.org/10.3390/su17062602

Keywords: mangrove stability; mangrove overturning; nature-based solutions; coastal protection

1. Introduction

Mangrove forests offer sustainable solutions for flood safety in the 21st century, gaining attention as alternatives or nature-based complements to traditional flood protection structures like breakwaters or embankments [1,2]. Similar to coastal defense structures, mangroves reduce waves [3–5], currents [6], and coastal erosion through sediment accumulation [7]. However, unlike hard coastal structures, mangroves can adapt to environmental changes [8], regenerating after damage [9] and adjusting to rises in the sea level by accumulating sediment and modifying their root systems [10]. Moreover, mangroves contribute to carbon sequestration [11], serve as nurseries for many fish species [12], and support local livelihoods [13]. Despite these advantages, mangrove forests cannot easily be implemented into coastal protection features yet as they lack design formulas like those used to predict the safety levels (i.e., failure chance) of engineered structures. Such formulas are needed to link extreme weather events to mangrove persistence (or failure). For instance, trees can fail during storms due to trunk breakage [14] or overturning [15], resulting in reduced wave attenuation [16,17], thus diminishing a forest's protective capacity. In addition, storm impacts like wind, erosion [18], burial [19], and inundation can damage mangroves and cause long-term mortality effects [9]. While attempts are being made to capture these failure mechanisms and implement them into design formulas, especially tree overturning mechanisms—where extreme canopy drag forces [20,21] overpower soil–root anchorage [22–24]—mangrove failure modes remain understudied. To assess mangrove resilience, it is hence necessary to unravel the components that enhance the resistance of mangrove trees to overturning during extreme weather events.

Ideally, mangrove tree overturning resistance would be measured directly in the field with tree loading experiments [25], where a winch is used to mimic wind loading and measure its impact on the root–soil system and stability of the tree. However, obtaining measurements of mangrove overturning in the field is challenging. Mangrove anchorage is a complex system with interacting environmental factors that can convolute overturning measurements. This includes, for instance, variations in soil properties, which can vary significantly within a single field site [26], or variations in root properties, like the architecture of aerial roots [27] and the spread and density of belowground roots, and material properties, such as root strength and flexibility [2]. Acquiring a sufficiently large dataset to develop design formulas would imply the destruction of large numbers of trees, while mangroves are already under threat in many places around the world [28]. Moreover, the purpose of this study is to ultimately use mangrove forests in sustainable nature-based coastal protection, which does not align with the destruction of many trees. As large-scale field measurements are not realistic, alternative approaches are needed.

The current study therefore aims to (i) serve as a pilot study to inform the design of future field experiments that investigate mangrove resistance to overturning, and to (ii) support the development of design formulas that capture mangrove tree overturning resistance. Using small-scale 3D-printed (Nylon 12) mangrove mimics, this study aims to assess which sediment and root properties require priority in field measurements, hereby minimizing the number of trees damaged for research purposes, and explore to what extent we can apply our knowledge of overturning terrestrial trees to mangrove trees, which grow in dynamic, water-logged sediments [29] and develop shallower roots [28]. The 3D-printed mangrove tree mimics were designed to represent the shallow belowground

portion of mangrove root systems of *Avicennia* and *Rhizophora* spp. We tested these mimics in sediment conditions representing natural contrasting mangrove sites. The mimics were geometrically scaled at 1:100 and the Nylon 12 material was selected for the trees and sediment densities to match those of natural trees and soils, ensuring that the measured forces were also scaled at 1:100 relative to the field conditions. Overall, our experiments aim to provide a first step towards understanding how root distribution influences mangrove stability across diverse soil conditions, while the strengths and limitations of this study are discussed.

2. Materials and Methods

2.1. Sediment Preparation and Properties

As mangroves can grow in diverse sedimentary environments, we aimed to cover the range of coastal sediments found in the literature (shown in Table S1). Based on this overview, we prepared five sediment types by mixing various sand, silt and water contents (Table 1). Each sediment was mixed with water, as dry sediment is not usually found at the seaward forest fringe, the zone where most uprooting takes place [30,31].

Table 1. The five sediment types we mixed and their properties, ordered by shear strength τs for easy comparison with the figures in Section 3.

Saturation State	Sediment	Sand Content (%)	Silt Content (%)	Average Grain Size (μm)	Water Content (% of Dry Weight)	Bulk Density ρ_s (kg m^{-3})	Penetration Resistance Pen_s (kPa)	Shear Strength τ_s (kPa)
Undrained	Silt	0	100	30	100	1498	0.5	0.7
Undrained	Sand	100	0	400	30	1732	64.3	7.6
Undrained	Silty sand	50	50	215	50	1738	6.5	9.1
Drained	Silt	0	100	30	70	1537	20.0	15.0
Drained	Silty sand	50	50	215	30	1903	53.7	40.7

We mixed homogenous sediments to ensure that our measurements were as consistent as possible. For sand, we used aquarium sand with a grain size of 0.2–0.6 mm (JBL Sansibar, Neuhofen, Germany). For silt, we used kaolin powder with a grain size of 25–35 μm ($Al_2Si_2O_5(OH)_4$, Colpaert–Van Leemputten, Nevele, Belgium). To characterize the properties of each mixture, we measured the bulk density ρ_s (kg m^{-3}), penetration resistance pen_s (kPa) and shear strength τ_s (kPa; Table 1).

The bulk density ρ_s was measured by weighing a disk filled with a known volume of sediment. The penetration resistance pen_s was measured by pushing down a 60° cone with a surface area of 50 mm^2 using a precise automated extenuator (INSTRON, Norwood, MA, USA) with a speed of 60 mm min^{-1}.

The sediment shear strength τ_s was measured by placing a plate with a diameter of 8 cm below a 0.7 cm layer of sediment (i.e., same size and depth as the mimics in the pulling test; Section 2.3) and pulling the plate upward with a speed of 60 mm min^{-1}. The maximum load before failure was used to calculate the sediment shear strength τ_s, where we first subtracted the weight of the root–sediment plate from the maximum load and then divided it by the surface area of the sediment edge (i.e., perimeter of the plate × depth of the plate).

2.2. Root Plate and Mimic Design

We designed mangrove mimics with 3D-printed roots for five root mass distributions (Figures 1 and 2b) and various root breakages (Figure 2b). The root mass distributions were

inspired by photos of uprooted or eroded mangrove roots of *Avicennia germinans*, *Avicennia alba*, and *Rhizophora stylosa* (shown in Figure 1a–c).

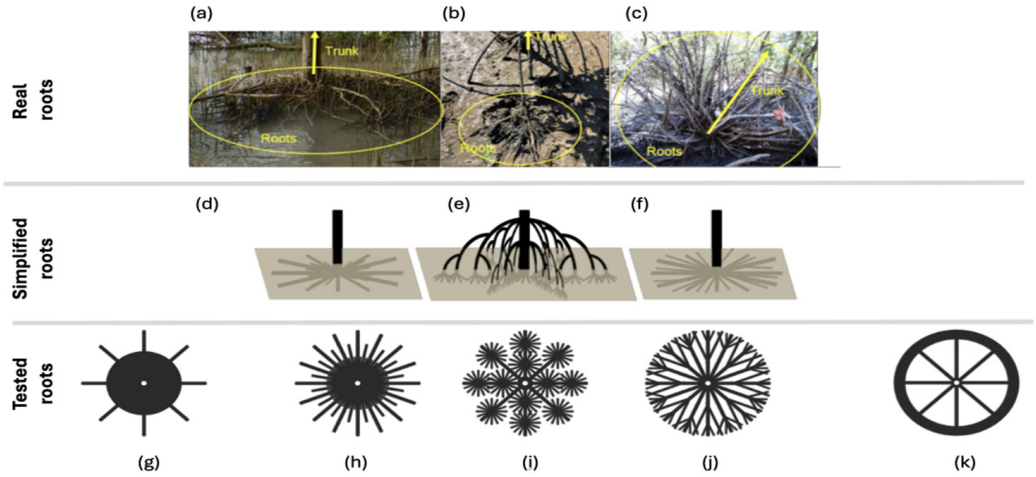

Figure 1. Resemblance between real mangrove root systems and the root mimics used in this study. Photos show root systems of mangrove trees, with (**a**) young *Avicennia alba* trees with root systems partially eroded after the 2017–2018 wet season in Sayung, Demak, Indonesia, (**b**) a *Rhizophora stylosa* sapling (~5yo) with an excavated stilt root in Hailing Island, China, in 2021, and (**c**) an uprooted *Avicennia germinans* tree along the central coast of the Gulf of Mexico in 2015. The schematized views (**d**–**f**) show what the entire anchorage root systems would roughly look like belowground. The bottom row shows the root plate designs that range from extreme (**g**,**k**) to more realistic (**h**–**j**), where the more realistic designs were inspired by the real mangrove root systems, while the extreme root systems allow us to study the extreme ends of the biomass distributions (close or far from the tree trunk). Photos taken by Celine van Bijsterveldt (**a**), Tianping Xu (**b**) and Alejandra Vovides (**c**).

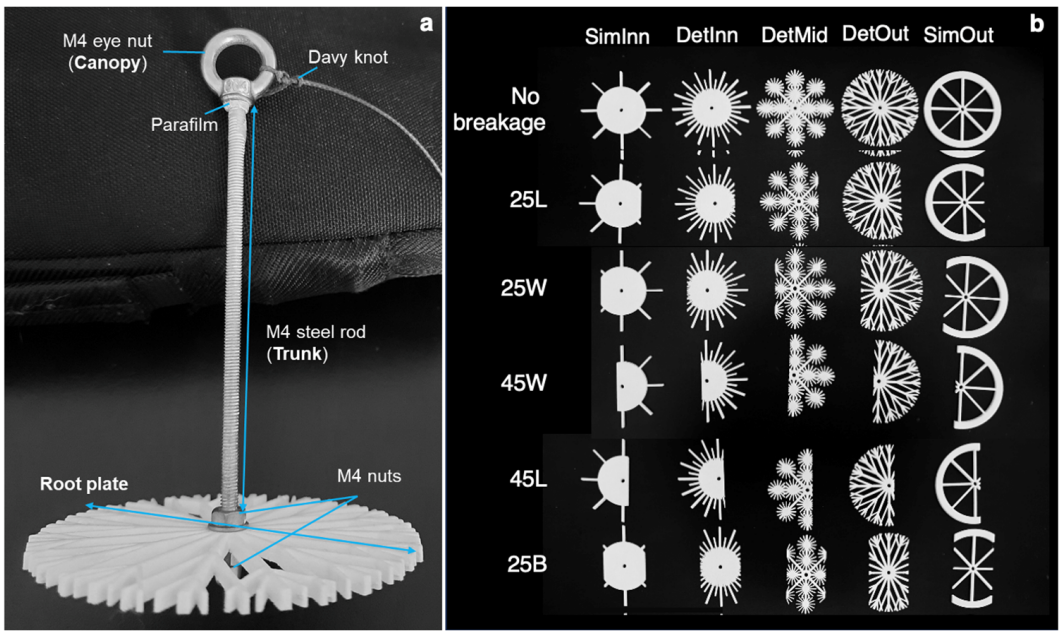

Figure 2. (**a**) Construction of a mangrove mimic, with a tree trunk made of a M4 stainless steel rod, a canopy made of a M4 stainless steel eye nut held firmly in place with parafilm, and a 3D-printed root plate held in place with nuts. The mimic and root plates are shown following the pulling direction used in the pulling tests. (**b**) The 3D-printed root plates, showing the five root mass distributions (where Sim = simple and Det = detailed), including breakage variations; no breakage, 25% or 45% root plate area loss, windward breakage (25WL, 25W), leeward breakage (25L, 45L), or breakage at both sides (25B).

We developed idealized versions for reproducible testing, with some more realistic and detailed (Figure 1h–j) and some more extreme and simplified root mass distributions (Figure 1g,k), to test the entire realm of possible root mass distributions, such that some have biomass closely centered around the stem (SimInn), some have biomass evenly spread out (DetInn, DetMid, DetOut), and some have biomass far away from the stem (SimOut). In this naming system, 'Sim' stands for simple and 'Det' stands for detailed.

The root plates were designed with equal surface areas A_r (Figure 2), but they differed slightly in their actual surface area because of the 3D printing process (Figure 3). Therefore, in this paper, the root plate areas A_r (cm^2) will be represented by the proxy root plate weight W_r (g).

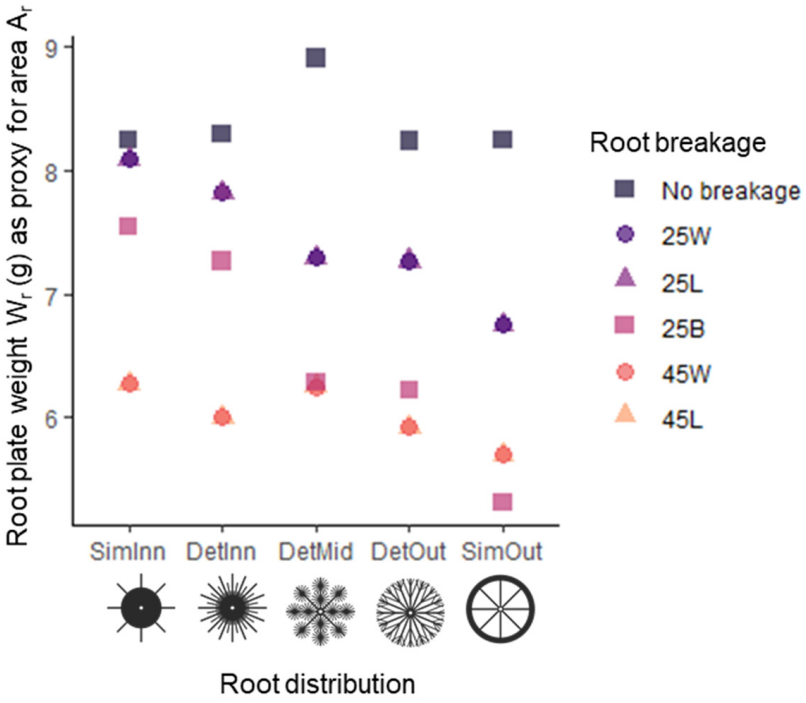

Figure 3. Root plate weight Wr (g), as a proxy for area Ar (cm^2), per root mass distribution and root breakage.

To assess the effect of root breakage, we removed a part of the root plate. We did this at two distances from the edge of the root plate, at 25% and 45% of the total diameter of the plate (2 and 3.5 cm of 8 cm diameter, respectively) and on the windward side (25W, 45W), leeward side (25L, 45L) or both sides (25B; Figure 2b). As the root distributions varied in the location of their biomass, the reduction in area (proxy weight W_r) was higher for some (e.g., SimOut) than for other root distributions (e.g., SimInn; Figure 3).

We opted to design rigid mangrove tree mimics that were scaled approximately 1:100 in terms of size compared to real mangrove trees (see Table 2), resulting in a root plate diameter of 8 cm and a height of 3 cm to facilitate the quick subsequent pulling tests.

2.3. Root Plate 3D-Printing Process and Assemblage

We drew the root systems using a browser-based 3D modelling program, namely Tinkercad (Autodesk, San Rafael, CA, USA), and 3D printed them with Nylon 12 plastic using Selective Laser Sintering (Shapeways, Eindhoven, The Netherlands).

The mimics were constructed by attaching the 3D-printed root plates with nuts to a tree trunk made of a M4 stainless steel rod and a canopy made of a M4 stainless steel eye nut held firmly in place with parafilm (Figure 2a). The Nylon 12 material has a density of 1.02 kg/m^3 and a tensile modulus of elasticity of 1800 N/mm^2 [32]. The 3D-printed mimics

did not deflect during the experiments and any flexibility effects can therefore be neglected in the interpretation of the results.

Table 2. Properties of mangroves trees and mimics, and mimics scaled up 100×. Tree data are from Njana et al. [33,34], where the root plate radius is based on the length of the belowground (cable) roots.

Tree/Mimic	Tree Height, m (Mean ± SD)	Root Plate Radius, m (Range)	Root Depth, m (Range)
Avicennia marina	9.6 ± 5.4	1.4–16.1	0.2–1.4
Rhizophora stylosa	7.4 ± 6.4	1.6–5.1	0.3–1.0
Mimic	0.105	0.04	0.007
Mimic upscaled 100×	10.5	4	0.7

2.4. Weight Scaling of Tree-Soil System

The geometric scaling of both the soil layer and trees also implies the weight scaling of both the soil and trees, since the density of the soil is natural, and the density of the mimic material (Nylon 12) is the same as that of mangrove trees (slightly above 1 kg/m^3). Since these experiments aimed to explore how varying sediment cohesions influence the failure of a block of rooted sediment, the sediment grain size was not scaled. Scaling the particle size would be relevant if we were entraining particles using a flow but is irrelevant in an experiment where the adhesion of a substance is key. To account for the effect of sediment consolidation, which modifies both weight and cohesion, a wide range of sediment weights and cohesion values were tested.

2.5. Pulling Tests to Measure Overturning Moments

We carried out pulling tests with all sediments, root mass distributions and root breakages. In total, 345 pulling tests were conducted. Each test was carried out three times, where we replaced the sediment in the pot after each test and placed the same mimic in it again (explained below). We carried out tests in each sediment type using each root mass distribution with the unbroken root plates (5 sediments × 5 root distribution × 3 repetitions = 75 tests).

Each pulling test was prepared by 'planting' the mimic in a pot filled with one of the sediments. An 80-micron plastic bag with a watertight seal (to avoid water leakage from sediments) was placed in a 9.6 cm tall pot made out of a PVC pipe with a diameter of 15.5 cm. The plastic bag was filled with sediment and levelled off evenly at the top. The pot had a 1 cm PVC disk at the bottom. To ensure that each mimic was placed at a 1 cm depth, we removed the disk so that the sediment 'sunk' 1 cm. The mimic was then placed on top of the sediment and the remaining gap was filled and levelled off evenly at the top, so that the mimic was now 1 cm belowground with an effective sediment depth of 7 mm (as the root plate was 3 mm tall, equal to 0.7 m belowground in the field; Table 2).

The mimics were attached to the pulling mechanism of a universal testing machine fitted with a 10 N load cell (INSTRON, Norwood, MA, USA) by tying a polyester string (with a diameter of 0.75 mm and a tensile strength of 17 kg; Paracord Nano, Atwood Rope MFG, Millersport, OH, US) to the 'crown' of the mimic (the eye nut) with a Davy knot (Figure 2a). The other side of the string was looped through a pulley that was placed at a distance of 45 cm and attached with a bowline knot to the universal testing machine (INSTRON, Norwood, MA, USA).

Pulling tests were carried out by moving the pulling mechanism upward, so that the mimic that was attached moved forward (Figure 4a). During each pulling test, we measured the load F (N) per extension ε (mm) continuously (Figure 4b) and pulled until

the windward side of the root plate was fully uprooted. The pulling mechanism moved upwards at an extension speed of 60 mm min^{-1}. The extension ε (mm) was converted to a mimic angle θ_M (°) that moved with approximately 0.5 ° mm^{-1} (i.e., 30° min^{-1}).

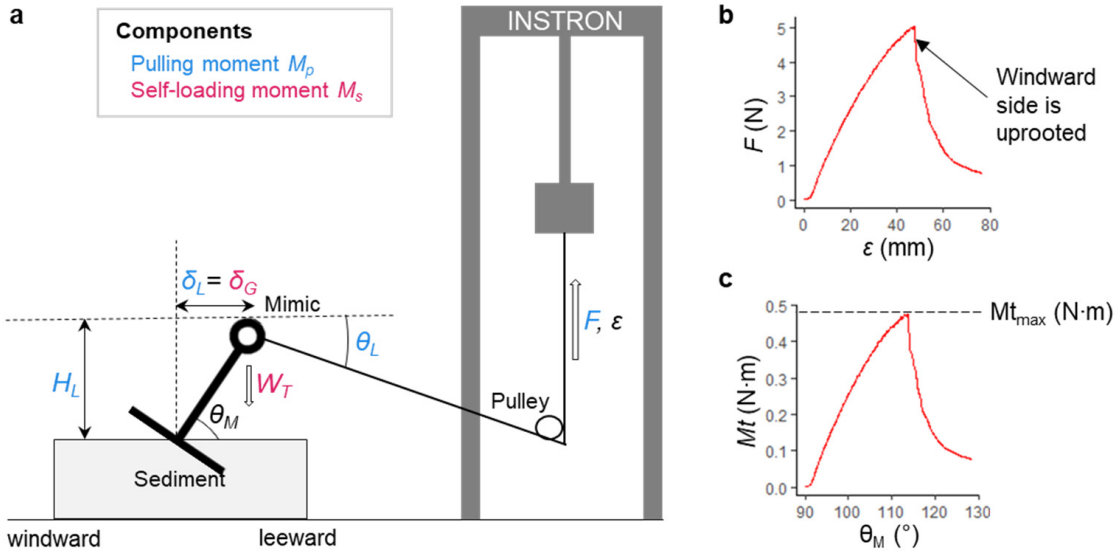

Figure 4. The pulling experiment, with (**a**) the pulling setup (not to scale) used to measure the overturning moment of each mimic using an INSTRON universal testing machine (INSTRON, Norwood, MA, USA), (**b**) an example of the output of a pulling test with load F (N) per extension ε (mm), which illustrates how the load (F) drops after the windward side is uprooted, and (**c**) an illustration of how we obtained the maximum overturning moment Mtmax (N·m). The calculation of the overturning moment Mt (N·m) is described in the text.

2.6. Calculation of Overturning Moments

We calculated the overturning moment M_t (N·m) according to Urata et al. [20]:

$$M_t = M_p + M_s \quad (1)$$

where M_p (N·m) and M_S (N·m) are the moments of the pulling load and self-loading (i.e., the turning moment generated by the weight of the mimic as it topples), respectively. The pulling load is the sum of its horizontal and vertical components:

$$M_p = H_L F cos\theta_L + \delta_L F sin\theta_L \quad (2)$$

where H_L is the pulling height (m), F is the pulling load (N), θ_L is the angle of pulling (rad) and δ_L is the horizontal displacement of the stem at pulling height (m). We calculated the pulling angle θ_L (rad) and the horizontal displacement of the stem at pulling height δ_L (m) using basic trigonometric calculations (Table S2). The self-loading moment M_s (N·m) is defined as follows:

$$M_s = \delta_G W_T g \quad (3)$$

wherein δ_G is the horizontal stem displacement at the center of gravity of the above-ground part (m), which is, in our case, the same as the horizontal displacement of the stem at pulling height δ_L (m); W_T is the aboveground biomass (kg); and g is the gravity (9.81 N kg^{-1}). An overview of all parameters can be found in Table A1 of Appendix A.

2.7. Statistical Methods

We used R (version 4.1.1) with packages rstatix (0.7.0), corrplot (0.92), FactoMiner (2.4), factoextra (1.0.7) and MuMIn (1.46.0) to carry out all statistical analyses. We calculated the maximum overturning moment Mt_{max} (N·m) as the highest overturning moment M_t (N·m) that was measured during a pulling test before failure, i.e., the moment just before the root plate was uprooted (Figure 4b). First, we tested the effect of sediment on mimic stability. We used a Kruskal–Wallis test to check if there were any significant differences in the maximum overturning moment Mt_{max} (N·m) between sediments; this was followed by a post-hoc Dunn's test to compare any differences between sediments.

We then tested the effect of root breakage on mimic stability. We normalized the maximum overturning moments Mt_{max} (N·m) for the sediment effect on stability by dividing the average Mt_{max} per sediment by the Mt_{max}. We then fitted, per sediment, a linear model between the normalized moments and root breakage, which was represented by the root plate weight W_r (g) as a proxy for the change root plate area A_r (cm^2), and we also calculated the Pearson correlation coefficient.

2.8. Mangrove Stability Model

We aimed to find out if mangrove (mimic) stability can be modelled mechanistically by adapting a model developed for terrestrial, shallow-rooted pine trees by Achim and Nicoll [22]. We used this model to predict the anchorage moment of our mangrove mimics and compared this to the measured maximum overturning moment Mt_{max}. Here, we assume that the maximum overturning moment Mt_{max} before failure is equal to the anchorage moment of the mimic.

We adapted this model at one point. In the original model, the resistance moment M_r is the resistance of the root–sediment matrix, which requires a resistance constant 'A_1' (N m^{-1}) to be estimated per sediment type based on the pulling tests. There is effectively no root resistance in our setup because the 3D-printed Nylon 12 material is too strong to break under the test circumstances, so that the only limiting factor is the resistance of the sediment.

Hence, we argue that the constant A_1 used in their model can be replaced with sediment resistance, measured as the sediment shear strength τ_s (N m^{-2}). Thus, we define the anchorage moment M_a as follows:

$$M_a = M_w + M_r \quad (4)$$

where M_a is the anchorage moment, M_w is the moment of the root–sediment plate weight and M_r is the moment of the root–sediment resistance. The moment representing the root–sediment plate weight is as follows:

$$M_w = y_1 W_s g \quad (5)$$

where M_W is the moment of the root–sediment plate, y_1 is the distance from the hinge to the center of gravity of the root–sediment plate (m; lever arm length, Figure 4), and W_s is the weight of the sediment in the root–sediment plate: $W_s = D_s A_r \rho_s$; here, A_r is the area of the root–sediment plate, D_s is the sediment depth, ρ_s is the bulk density of the sediment (kg m^{-3}) and g is the gravity (9.81 N kg^{-1}). Furthermore,

$$M_r = \tau_s D_s C_p y_2 \quad (6)$$

where τ_s (N m^{-2}) is the sediment shear strength (as measured in Section 2.1), D_s (m) is the sediment depth, C_p (m) is the circumference/perimeter of the windward edge of the

root–sediment plate, and y_2 (m) is the distance from the hinge to the center of gravity of the arc (Figure 4 and Table S2).

To assess the model fit of the anchorage model (Equation (4)), we compared the predicted anchorage moment M_a to the observed maximum overturning moment Mt_{max} for the full anchorage model M_a (Equation (4)), the weight model M_w (Equation (5)) and the resistance model M_r (Equation (6)). For each of these models, we compared the Akaike information criterion (AIC) and Akaike weight [35], correlation r, intercept β_0 (which should be 0 for a perfect prediction) and slope β_1 (which should be 1 for a perfect prediction). For the best-fitting model, we then left out each of the non-constant model components (e.g., for the resistance model, leave out τ_s, then C_p, then y_2) to assess the role of each component.

3. Results

3.1. General Patterns in Mimic Stability

The overturning curves varied between sediment types, root mass distributions and root breakage (Figure 5). The maximum overturning moment withstood by the soil–root system (proxy of tree stability) was largest for drained soils with a low water content and a relatively larger sediment size. This can be seen in the larger stability values for Drained Silty Sand compared to the smaller values for Undrained Silts in Figure 5. The relationship between tree stability and the sediment type has been explicitly illustrated in Figure 6, which shows how the maximum overturning moment increases with the sediment shear strength.

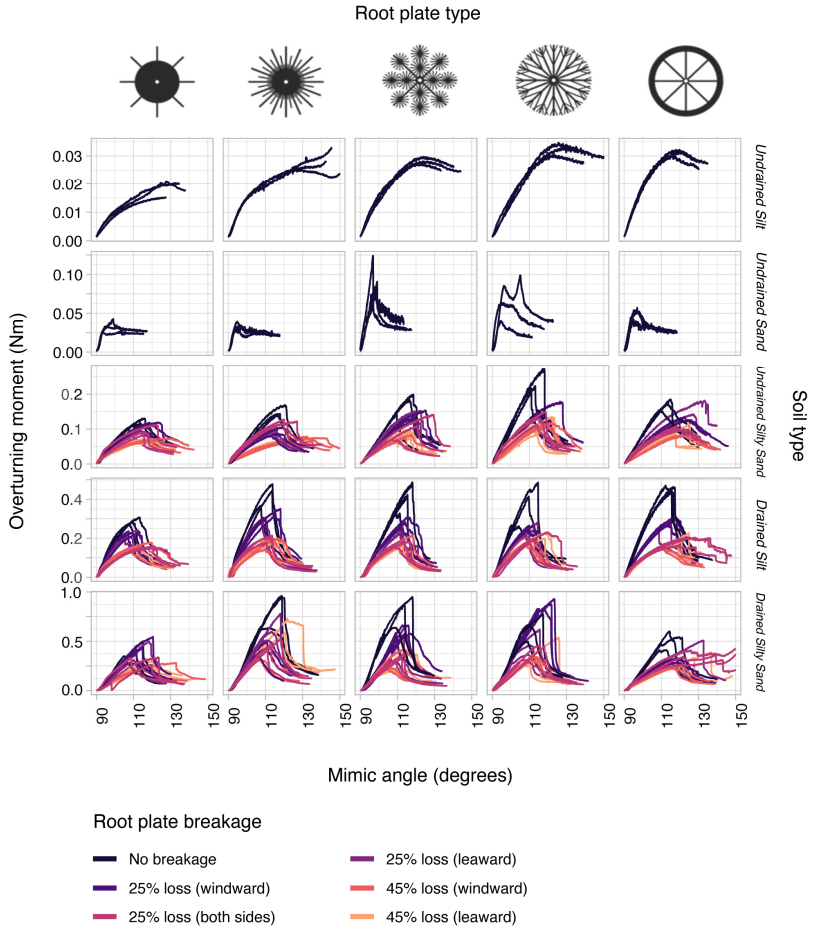

Figure 5. Overturning curves showing overturning moment (N·m) per mimic angle (degrees) for each root type and sediment. Note that there are different y-axes between sediments. Breakages were half (25% of the complete plate) or complete.

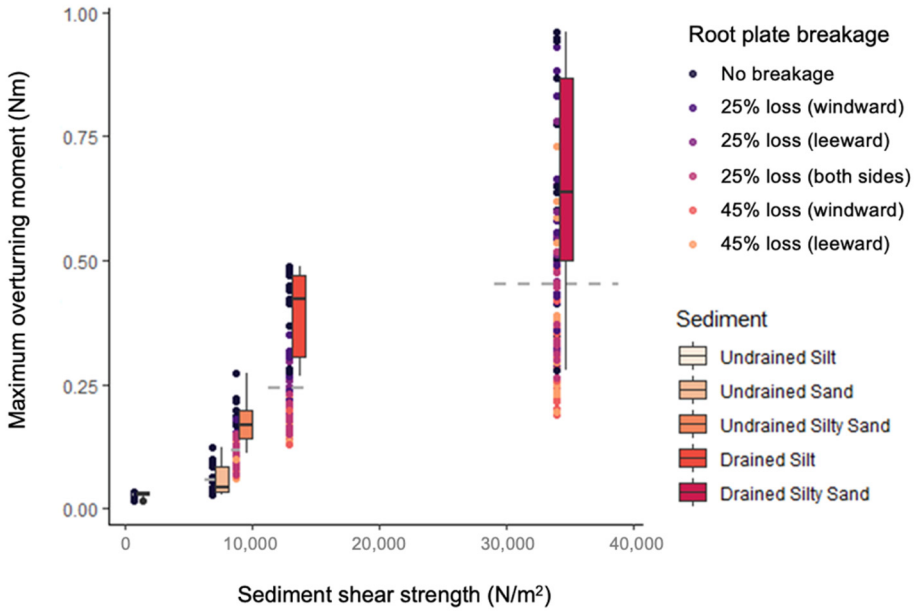

Figure 6. Effect of sediment type on mimic stability, showing maximum overturning moment (N m) per sediment shear strength (N m^{-2}), shown for all root mass distributions and breakages. Points show all data and are shown at the exact mean shear strength, while the boxplots are dodged. The boxplots only show data for the non-broken root systems, as Undrained Silt and Undrained Sand were not tested with broken roots. The dashed line indicates the standard deviation of the shear strength measurements. Breakages were half (25% of the complete plate) or complete (45%) breakage at the windward, leeward, or both sides of the root plate (see Figure 2b).

The distribution of the belowground root plate also significantly influences the resistance of mangroves to overturning but, interestingly, the optimum (most stable) distribution changes per sediment type (Figure 5). For instance, root systems where cable roots spread radially from the center (DetOut) are most stable in relatively weak soils (Undrained Silt). For stronger sediments (Drained Silty Sand), root systems that increase their biomass near the center of the root system show higher stability (like DetInn).

There is a limit on increasing biomass near the center, though, as the root system with the most condensed biomass near the center (SimInn) is the least stable in all soil types. This implies that *Avicennia sp.* trees, which inspired the schematized root systems, DetInn and DetOut, could increase their stability in weak soils by spreading their biomass (DetOut) and increase their stability in stronger sediments by developing biomass closer to the center in stronger soils (DetInn) until reaching an optimum root configuration.

Figure 5 also suggests that the belowground root plate inspired by *Rhizophora* sp. trees is relatively more advantageous in terms of stability compared to the other root systems, due to its well-drained sandy soils. Moreover, the stilt roots of *Rhizophora* sp. mangroves could increase their stability even more with respect to the results of Figure 5 (see Section 4). Overall, these results suggest that mangroves could adjust their root plate morphology to the sediment they grow in to maintain optimal stability, as previously observed for various terrestrial tree species [36].

The pulling experiments also support that root plates with a larger area increase tree stability, implying that the breakage and detachment of part of the root system largely reduce stability, as shown in Figure 7. The role of breakage seems to be relatively more relevant for better drained soils, as indicated by the steeper curves for Drained Silt and Drained Silty Sand compared to Undrained Silty Sand.

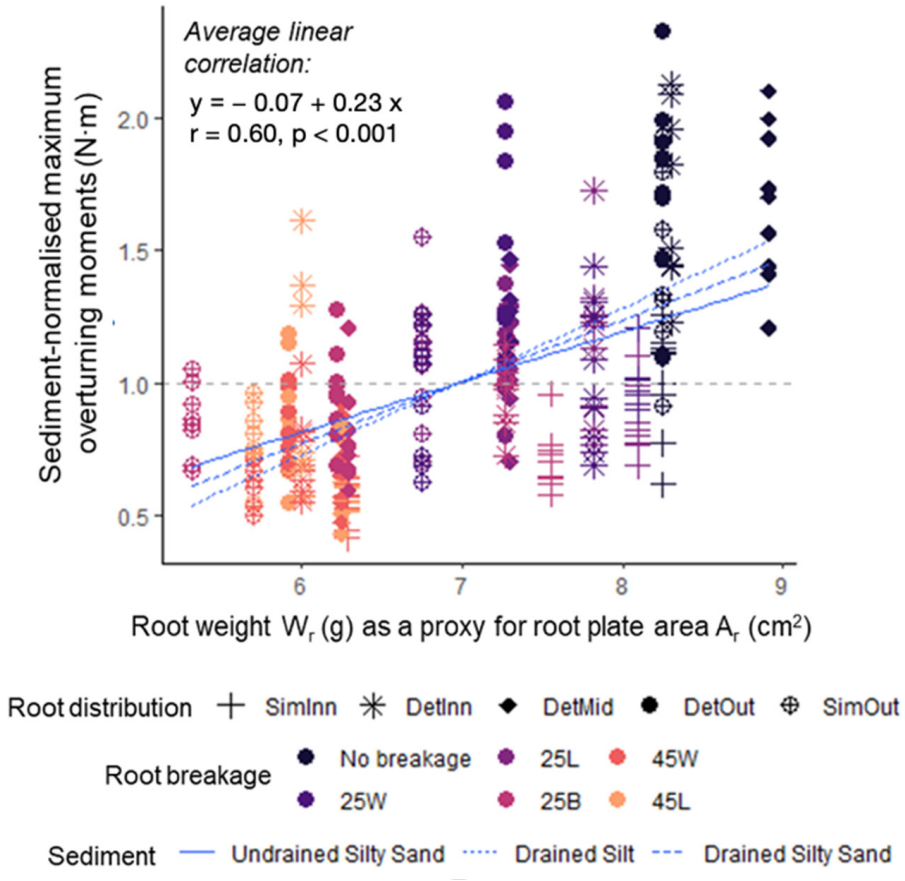

Figure 7. Effect of root breakage on mimic stability, with sediment-normalized maximum overturning moment Mtmax (N·m) per root weight Wr (g) as a proxy for surface area Ar (cm^2), tested in Undrained Silt Sand, Drained Silt and Drained Silty Sand. Blue lines indicate the Pearson correlation between the root weight Wr and the sediment-adjusted maximum overturning moment Mtmax.

3.2. Anchorage Predictions and Model Fitting

We compared the measured maximum overturning moments M_{tmax} (N·m) to the anchorage moments M_a (N·m) predicted with the anchorage model (Equation (4)) and found that the resistance model M_r (Equation (6)) best fit our data (Table 3). Furthermore, we observed that the model overestimated stability slightly in most cases, such that the average ratio $Mt_{max}/M_a = 0.71$ (Figure 8). The model's accuracy was quite variable across sediment types, but was more consistent for root breakage (Figure 8a,b). Across root mass distributions, the model was more accurate for more widespread distributions (Figure 8c).

Table 3. Parameters of mechanical model variations. The sediment depth Ds and gravitational constant g are constants and not considered in the calculated df.

Prediction Equation	df	AIC (M_t~M_a)	W_i	r ($p < 0.01$)	β_0	β_1
$M_a = y_1 W_s g + \tau_s D_s C_p y_2$	5	−507.08	0.06	0.84	0.03	0.56
$M_a = y_1 W_s g$	2	−153.08	0	0.2	0.17	14.07
$M_a = \tau_s D_s C_p y_2$	3	−512.6	0.94	0.84	0.04	0.56
$M_a = \tau_s D_s y_2 l$	2	−491.76	0	0.83	0.03	0.07
$M_a = D_s C_p y_2$	2	−145.53	0	0.13	0.18	3065.44
$M_a = \tau_s D_s C_p$	2	−433.52	0	0.79	0.03	0.02

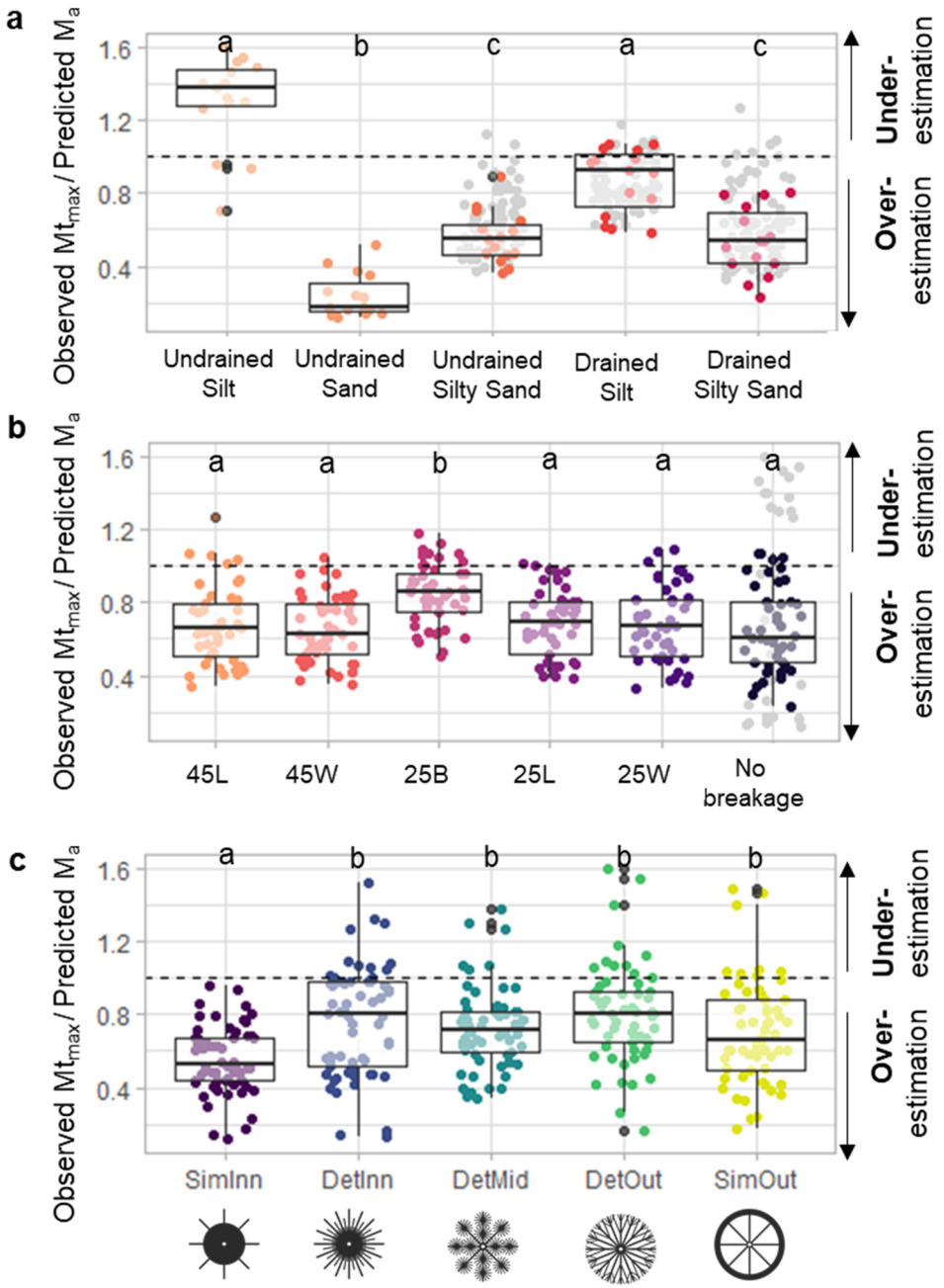

Figure 8. Jitterplots and boxplots of model fit for (**a**) sediment types, (**b**) root breakage and (**c**) root distributions. Colored dots represent the data used in the boxplots. Grey dots represent the entire dataset but are excluded as not all root breakages were tested in all sediments. The dashed lines indicate an accurate prediction. The significance letters for boxplots ($\alpha = 0.05$) were obtained according to Dunn's test. Breakages were half (25% of the complete plate) or complete (45%) breakage at the windward, leeward, or both sides of the root plate (see Figure 2b).

4. Discussion

In this study, we aimed to understand the effect of the sediment type, root mass distribution and root breakage on mangrove tree stability using 1:100-scaled 3D-printed mimics. We observed higher mimic stability with a higher sediment shear strength and larger root plates (i.e., with less mimicked root breakage). Moreover, we found that the optimal root distribution for stability depended on the sediment type, and that the effect of root breakage on mimic stability also depended on the sediment type. Finally, we showed that the mechanistic anchorage model developed for terrestrial trees provided

useful mechanistic principles for estimating mangrove tree stability, with the specification of the sediment resistance through the sediment shear strength being a useful alteration to this model.

4.1. Strengths and Limitations of the Experimental Set Up

Given the limited existing research on mangrove overturning, we used schematized root systems to isolate overturning processes, starting with the belowground root distribution. While being oversimplified, this approach does enable us to (i) derive the first generic patterns for shallow rooting mangrove species, and (ii) test the applicability of a terrestrial tree model for mangrove-like root systems. Future studies could incorporate additional processes and gradually increase complexity. Aerial roots were omitted in this study, but they can play a key role in stability; for example, Hill et al. [37] found that detaching aerial roots from the soil halved the force required to tilt a *Rhizophora stylosa* tree. Mangrove canopies are often offset from the trunk due to competition and wind stress [38], which also alters the overturning moment—a factor that could be investigated in future experiments. Follow-up studies could investigate materials that replicate not only the density but also the strength of natural mangrove roots to test root failure. Future studies could also include prototypes with multiple trees and varying root interconnection between trees, as intertwined roots may enhance overall forest stability [39].

A key limitation in developing mimic designs is the scarcity of studies mapping belowground mangrove root systems. Field surveys of fallen trees, like those by van Bijsterveldt et al. [10], could help expand our database of root typologies. Advanced tools like laser scanners and radars could map both the aboveground and belowground root systems of healthy trees. Comparing the root systems of healthy and fallen trees after storms, along with sediment sampling at fallen tree sites, could reveal the factors contributing to vulnerability. Additionally, field measurements could highlight species-specific differences in the extent of roots (as those presented in Table 2) and their impact on mangrove stability.

4.2. Validation with Field Experiments

Field tree-pulling experiments are recommended to validate the behaviors observed in scaled experiments. Scaled experiments could in turn guide the selection of environments and trees, focusing on root and soil types with distinct behaviors. A systematic approach—such as starting with a specific species or multiple species in a single soil type—can help minimize confounding factors. This ensures that the lessons learned from destructive field studies are more easily extrapolated to model development and enhance our conceptual understanding of tree stability.

4.3. Additional Drivers of Mangrove Root Development

Our experiments testing a root plate with a constant radius revealed that the most stable root configuration depended on the sediment type, consistent with findings for terrestrial trees [36]. However, factors beyond sediment type also influence root development. For instance, wind loading can induce thigmomorphic growth, increasing root mass on the leeward side [40], and waterlogging can inhibit root growth while promoting eutrophication shoots [41,42]. To better understand mangrove stability in coastal environments, field studies are needed to investigate the factors that influence the belowground root morphology of various mangrove species.

4.4. Failure Models

The mechanistic tree stability model for terrestrial trees by Achim and Nicoll [22] predicts mimic anchorage with reasonable precision (see AIC comparisons in Tables 3

and A2) and provides simple, useful principles for understanding mangrove stability. However, the model excludes root–sediment resistance and does not differentiate between root distributions. As a result, it cannot account for the effective windward perimeter (*Cp*) and leeward arm (*y2*) (see Figure A1 in the Appendix A), which vary with sediment type and root morphology interactions. Field validation with mangroves is needed to assess the model's reliability across different sediment types, root morphologies, and species.

4.5. Implications for Mangrove Stability in Coastal Settings

Our experimental data revealed the strong influence of the sediment's shear strength on mimic stability, with greater stability observed in sediments with higher upward shear strength, consistent with findings for terrestrial trees [43,44]. Since waterlogged sediments generally exhibit lower shear strength [45], mangrove trees at the seaward fringe, where waterlogging is more frequent or prolonged, may be less stable.

Mangroves rooted in waterlogged, silty, or clayey sediments—which erode more easily [46]—are at a higher risk of overturning compared to those in sandy sediments. When present in shallow sediments (0.1 m depth), *Rhizophora* species have been observed to produce more prop roots [47], which increases their belowground biomass and stability. By trapping sediment [9], mangroves can potentially enhance their root depth and protect against erosion and uprooting. The impact of soil depth on tree stability is further discussed in the following section.

4.6. Frameworks to Implement Mangrove Failure in Coastal Protection

This study provides a critical foundation for estimating vegetation failure in nature-based or hybrid flood protection systems, such as embankments combined with mangrove forests. Our findings suggest that stability models for terrestrial trees can be adapted for mangroves, though additional processes (discussed earlier) must be explored, and field validation is essential before application.

Once validated with field data, these failure models could predict tree instability during storms using Equations (4)–(6) and various forest data, including the species distribution, height, surface area, root dimensions, and local sediment characteristics. These equations can complement existing wave reduction models, such as those by Mendez and Losada [48], by accounting for vegetation failure and its impact on wave attenuation. Similarly, mangrove failure formulations could be applied using the output of wind models.

The wave heights propagating through damaged forests can then inform the design of coastal protection structures, such as revetments for embankments. As illustrated in Figure 9, neglecting mangrove failure due to wind and waves in design calculations risks underestimating the structural requirements, potentially compromising the flood safety of the hinterland.

Lastly, Equations (4)–(6) can be integrated into models estimating the changes in bed level (sediment) that occur during storms to assess how tree stability varies under extreme conditions. For example, in Figure 10, we used these equations to demonstrate the influence of sediment depth on tree stability, expressed through the anchorage moment provided by vegetation. The results indicate that greater root depths (i.e., a sediment layer with a greater thickness over the root plate) enhance mangrove stability by increasing the anchorage moment.

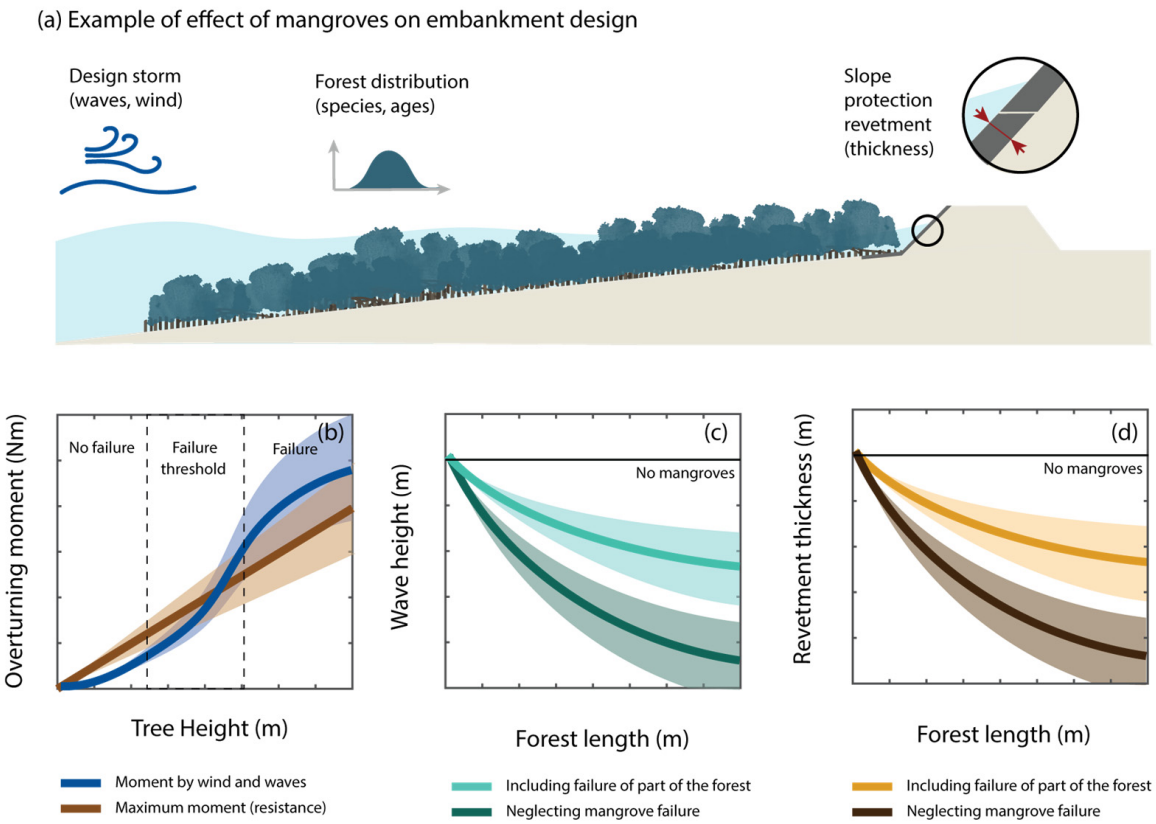

Figure 9. Example of conceptualized effects of mangrove failure on embankment designs and the required thickness of the slope revetment. (**a**) Given a forest distribution (in terms of species, ages, and geometry of the different trees) and the design conditions of a coastal embankment (wave heights, wave periods, water levels, wind speeds), (**b**) assessing the stability of mangroves against overturning requires the load acting on the trees (overturning moment due to wind and/or waves) to be compared with the resistance of individual trees (which will depend on their species, age, geometry). (**c**) Mangroves can reduce wave loads, but the partial/full failure of the forest (e.g., if a percentage of the forest collapses) would diminish the wave attenuation capacity of the mangrove system. (**d**) Neglecting this failure could imply that a design element, in this case the thickness of the slope revetment, is under-dimensioned, leading to the failure of the structure during the designed storm conditions.

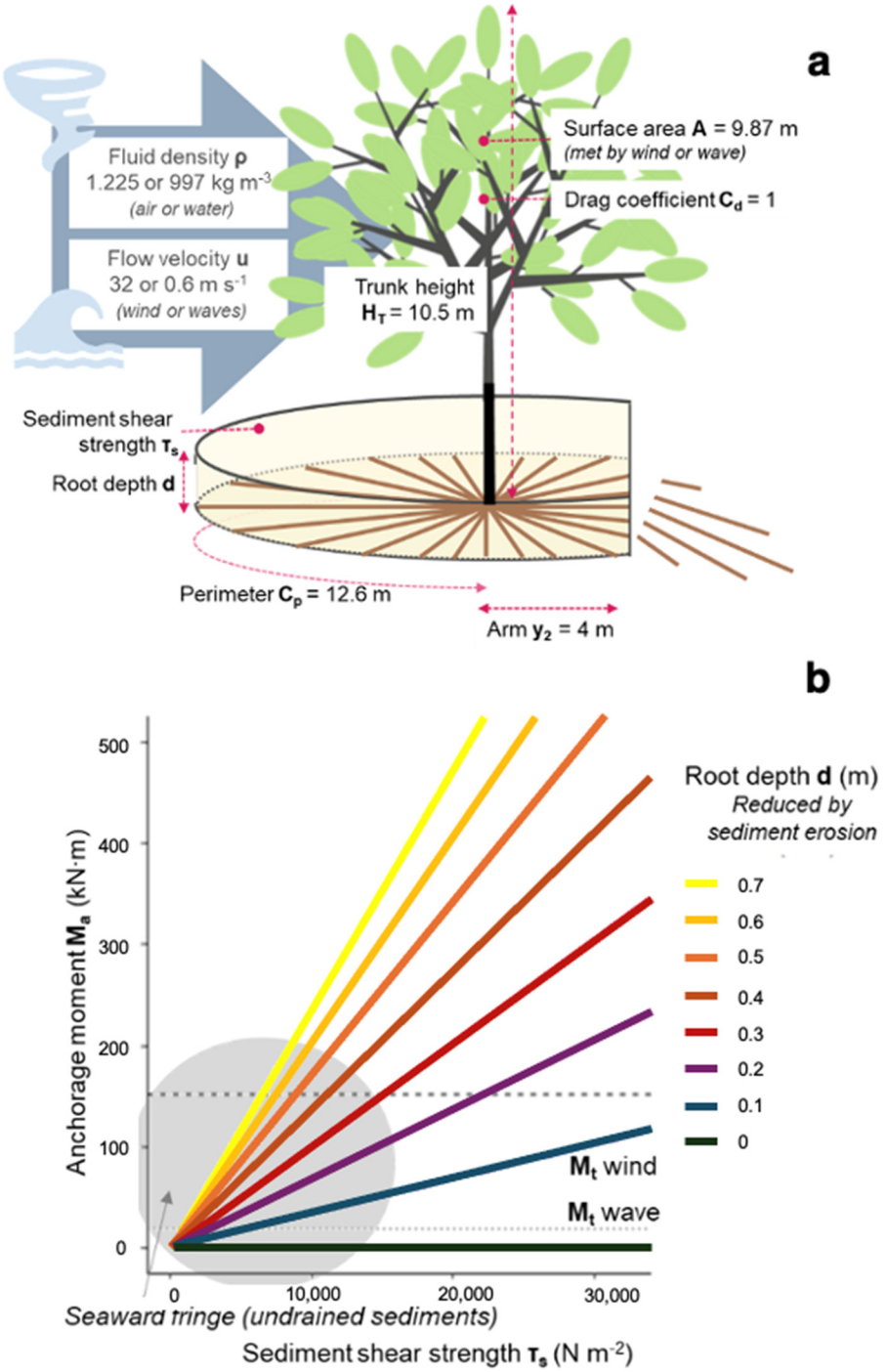

Figure 10. Simplified example of mangrove tree stability estimation for various root depths Ds and sediment shear strengths τs, assuming that the true parameter values are known. (**a**) Variables required to estimate overturning moments and tree resistance, and (**b**) estimates of the anchorage moment (resistance) of mangrove trees as a function of the sediment shear strength. The resistance model is used to estimate anchorage [22] and the drag model is used to estimate the overturning moment [49]. If the overturning moment Mt becomes larger than the anchorage moment Ma, the tree loses its stability. Value sources are listed in Table S4.

5. Conclusions

Our study provides valuable insights into the factors influencing mangrove tree stability under storm conditions. The results show that tree stability is strongly influenced by the sediment type, with drained soils offering higher stability due to an increased shear strength. The root mass distribution also plays a critical role, with optimal configurations varying depending on the soil conditions—the radial spread of roots enhances stability in weaker soils, while concentrated biomass is more beneficial in stronger soils. Additionally, larger root plate areas improve stability, highlighting that a reduction in stability is caused by root breakage. The anchorage model developed in this study provided reasonable predictions of the overturning moments, though it slightly overestimated the stability in most cases. These findings suggest that mangroves can adjust their root morphology to optimize their stability in response to varying soil conditions, offering a foundation for future research and applications in coastal protection systems. This study has limitations, notably the exclusion of aerial roots and root intertwining, which are crucial for mangrove stability. Future research should explore the effects of wind loads and waterlogging on root development and include field tree-pulling experiments to validate our findings. Expanding the database of root systems using field surveys and advanced mapping techniques could provide valuable insights into species-specific root morphology and stability, helping guide more complex future models.

Supplementary Materials: The following supporting information can be downloaded at: https://www.mdpi.com/article/10.3390/su17062602/s1, Figure S1: Parameters used to calculate H_L and θ_L and $\delta_{L,}$, figure adapted from Figure 4; Table S1: Mangrove sediment composition reported in the literature; Table S2: Calculation to obtain parameters values for H_L and θ_L and $\delta_{L,}$ needed for Equations (2) and (3); Table S3: Values used to calculate anchorage (see Equations (4)–(6)); Table S4: Values used to calculate critical overturning forces and critical wind and wave speeds [49–56].

Author Contributions: Conceptualization, R.v.H. and M.K.; methodology, R.v.H. and M.K.; validation, R.v.H., formal analysis, R.v.H., writing—original draft preparation, R.v.H., A.G.M., M.K., C.E.J.v.B., J.d.S., J.v.B., B.W.B. and B.H., writing—review and editing, A.G.M.; visualization, R.v.H. and A.G.M.; supervision, T.J.B.; project administration, T.J.B.; funding acquisition, Z.H. All authors have read and agreed to the published version of the manuscript.

Funding: The authors gratefully acknowledge financial supports of the Joint Research Project: NSFC (51761135022), NWO (ALWSD.2016.026), and EPSRC (EP/R024537/1): Sustainable Deltas, and of the Innovation Group Project of Southern Marine Science and Engineering Guangdong Laboratory (Zhuhai) (No. 311020003), Guangdong Provincial Department of Science and Technology (2019ZT08G090) and Fundamental Research Funds for the Central Universities of China (20lgzd16). The presented data are available at 10.5281/zenodo.7100977.

Institutional Review Board Statement: Not applicable.

Informed Consent Statement: Not applicable.

Data Availability Statement: The data presented in this study are available on request from the corresponding author.

Acknowledgments: We thank Nick Wang, Amy Taylor, Oliver Raven, Lennart van IJzerloo, Daniël Blok and Tianping Xu for their help with earlier iterations of the tree stability experiments, Johan van Hespen for his insights regarding 3D printing, Mohammed Al-Romaithy for sharing his knowledge on mechanics and Greg Fivash for calculating the root mass distribution parameter.

Conflicts of Interest: The authors declare no conflicts of interest.

Appendix A

Appendix A.1. Additional Information for the Methods

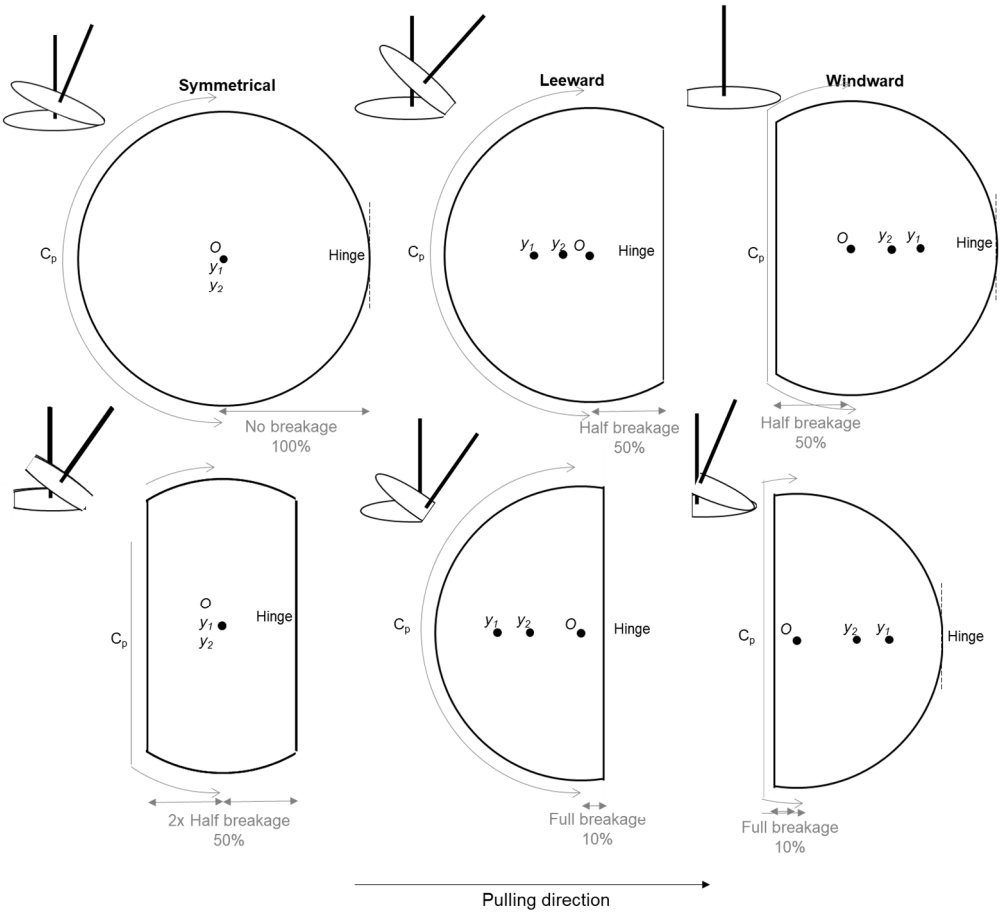

Figure A1. Hinges, centroids y1 and y2 (where we use the distance from the hinge to the centroids), and windward perimeter Cp for each of the root cuts, where we assume that they do not vary between the five different root mass distributions. Values can be found in Table S3.

Table A1. All properties with symbols, units, their meaning and the source where the values can be found.

Symbol	Unit	Meaning	Source
Soil parameters			
τ_s	N m^{-2}	Shear strength	Table 1
ρ_s	kg m^{-3}	Bulk density	Table 1
pen$_s$	N m^{-2}	Penetration resistance	Table 1
Root parameters			
P_r	%	Half surface parameter	Figure A2a
piv$_b$	#	Number of root breakages	Figure 2b
A_r	m^2	Root plate area	Figure 3, Table S3
W_r	kg	Root plate weight, proxy for area A$_r$	Figure 3, Table S3
D_s	m	Sediment/rooting depth	0.007; Table 2
Overturning components			
M$_t$; Mt$_{max}$	N m	(Maximum) overturning moment	$M_t = M_p + M_s$
M$_p$	N m	Pulling moment	$M_p = H_L F cos\theta_L + \delta_L F sin\theta_L$
M$_s$	N m	Self-loading moment	$M_s = \delta_G W_T g$

Table A1. *Cont.*

Symbol	Unit	Meaning	Source
H_L	m	Pulling height	See Figure 4a
F	N	Pulling load	See Figure 4a
θ_L	rad	Angle of pulling	See Figure 4a
δ_L, δ_G	m	Horizontal displacement of the stem at pulling height	See Figure 4a
W_T	kg	Aboveground biomass	0.02
Anchorage components			
M_a	N m	Anchorage moment	$M_a = M_w + M_r$
M_w	N m	Weight moment	$M_w = y_1(W\|\|r + W_s)g$
M_r	N m	Resistance moment	$M_r = \tau_s D_s C_p y_2$
y_1	m	Distance from hinge to the center of gravity of root–sediment plate	Table S3, Figure A1 of the Appendix A
W_s	kg	Weight of the sediment cylinder above the roots	$W_s = D_s A_r \rho_s$
g	N kg^{-1}	Gravitational constant	9.81
C_p	m	Perimeter of windward side of the root plate	Table S3, Figure A1 of the Appendix A
y_2	m	Distance from hinge to the center of gravity of the arc	Table S3, Figure A1 of the Appendix A

Appendix A.2. Additional Explanations and Results of Statistical Analyses

Appendix A.2.1. Additional Methods

To assess the role of root distribution in mimic stability, we calculated a parameter to describe the root distribution: P_r (%). The root distribution P_r was calculated by finding out at what distance from the trunk 50% of the cumulative biomass was reached. We then fit a polynomial regression model between the maximum overturning moment Mt_{max} (N·m) and the root distribution parameter P_r, per sediment type.

Then, we carried out a Principle Component Analysis and Pearson correlation tests to assess the effect of sediment properties (shear strength τ_s, bulk density ρ_s, penetration resistance pen_s), root distribution (P_r) and root breakage (number of breakages piv_b, root plate area A_r, root plate weight W_r as a proxy for area, C_p, y_1, y_2) on the maximum overturning moment Mt_{max}. Based on this analysis, we selected the best fitting parameters per variable group (sediment, root distribution, root breakage), and fit the linear and interaction models to the data. We compared the models using the Akaike Information Criterium (AIC) and Akaike weights (W_i) to find the best-fitting model (Johnson and Omland, 2004 [35]).

Appendix A.2.2. Additional Results

To test the effect of root mass distribution on mimic stability, we fitted a polynomial curve to the maximum overturning moment Mt_{max} across the root mass distributions per sediment. For this, we defined a root distribution parameter: P_r (Figure A2a). This confirmed the effect of root mass distribution, where the optimal root mass distribution depended on the sediment type (Figure A2b).

To investigate the size of the effect of these stability components and their interactions, we first carried out a principle components analysis and tested the linear correlations between all quantitative sediment and root plate variables (Figure 1). We found that the first three principle components accounted for 79% of the variation. In Principle Component 1, we observed the strongest correlation between the maximum overturning moment Mtmax and the root weight Wr (proxy for root area, Ar); in Principle Component 2, we observed the strongest correlation between the maximum overturning moment Mtmax and sediment shear strength τs. In Principle Component 3, we did not observe a

significant linear correlation between the maximum overturning moment Mtmax and the root distribution parameter Pr. Then, we carried out a model selection to analyze the role of the sediment shear strength τs and root weight Wr as a proxy for the root plate area Ar, the root distribution parameter Pr (as a polynomial), and their potential interactions (Table A2). The model with the lowest Akaike Information Criterium was Mtmax ~ τ_s+ W_r + τ_s : W_r + Pr2 + τ_s :Pr2+ W_r :Pr2 (AIC = −526.62). The parameter that best explained the variation in Mtmax was the sediment shear strength τs, followed by the root weight Wr (proxy for root area), and then the interaction between the two. Thus, if roots break, the change in stability depends on the sediment shear strength.

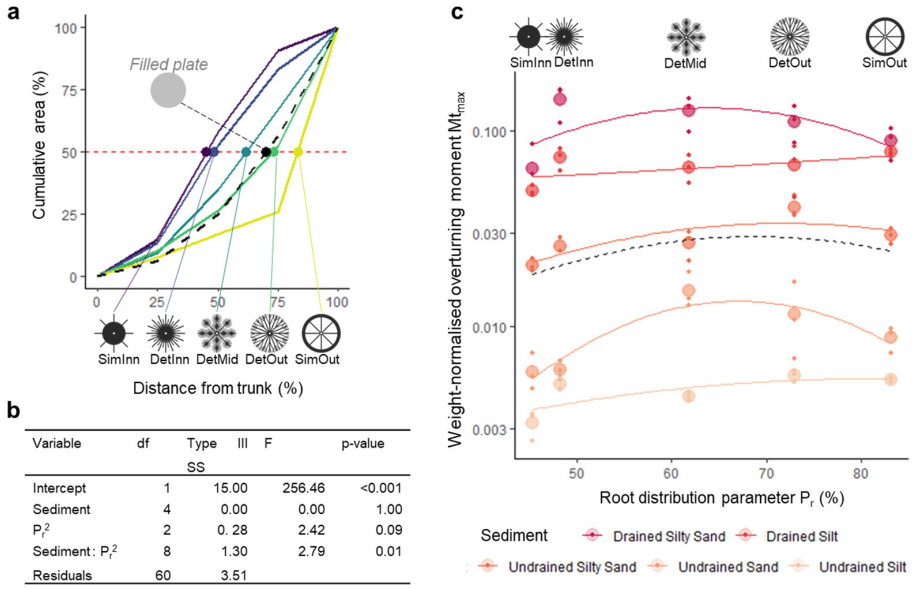

b

Variable	df	Type III SS	F	p-value
Intercept	1	15.00	256.46	<0.001
Sediment	4	0.00	0.00	1.00
P_r^2	2	0. 28	2.42	0.09
Sediment: P_r^2	8	1.30	2.79	0.01
Residuals	60	3.51		

Figure A2. Effect of root mass distribution on mimic stability, with (**a**) root distribution parameter Pr as the point where the cumulative surface area of the root plate reaches 50% (only for unbroken root plates), (**b**) ANOVA for the polynomial interaction model Mtmax~Sediment * Pr2 (dashed line in c); and (**c**) weight-normalized maximum overturning moment Mtmax (small dots) and mean moments (large dots) per root distribution Pr (%), shown per sediment for all non-broken roots. Mtmax is normalized for the root plate weight Wr as a proxy for the root plate area Ar to account for the small variations in surface area from the printing process (Figure 3); Mtmax/Wr. Showing only non-broken roots.

Table A2. Model comparison, showing model fits with Akaike Information Criterium AIC, Akaike weights Wi. and adjusted R2 with its p-value. Note that the root plate weight Wr functions as a proxy for the root plate area Ar.

Statistical Model	df	AIC	W_i	Adj. R^2	*p*-Value
Mt_{max}~1	2	−142.78	0	0	NA
Mt_{max} ~ τ_s	3	−399.28	0	0.58	<0.001
Mt_{max} ~ W_r	3	−146.48	0	0.02	0.017
Mt_{max}~P_r^2	4	−142.9	0	0.01	0.13
Mt_{max} ~ τ_s+W_r	4	−451.16	0	0.64	<0.001
Mt_{max} ~ τ_s+ P_r^2	5	−405.13	0	0.59	<0.001
Mt_{max}~τ_s+ W_r + τ_s : W_r	5	−490.85	0	0.69	<0.001
Mt_{max}~τ_s+ W_r + P_r^2	6	−466.51	0	0.66	<0.001
Mt_{max}~τ_s+ W_r + τ_s : W_r + P_r^2	7	−513.12	0	0.71	<0.001
Mt_{max}~τ_s+ W_r + τ_s : W_r + P_r^2 + τ_s :P_r^2	9	−519.52	0.03	0.72	<0.001
Mt_{max}~τ_s+ W_r + τ_s : W_r + P_r^2 + W_r :P_r^2	9	−516.17	0.01	0.72	<0.001
Mt_{max}~τ_s+ W_r + τ_s : W_r + P_r^2 + τ_s :P_r^2 + W_r :P_r^2	11	−526.62	0.97	0.73	<0.001

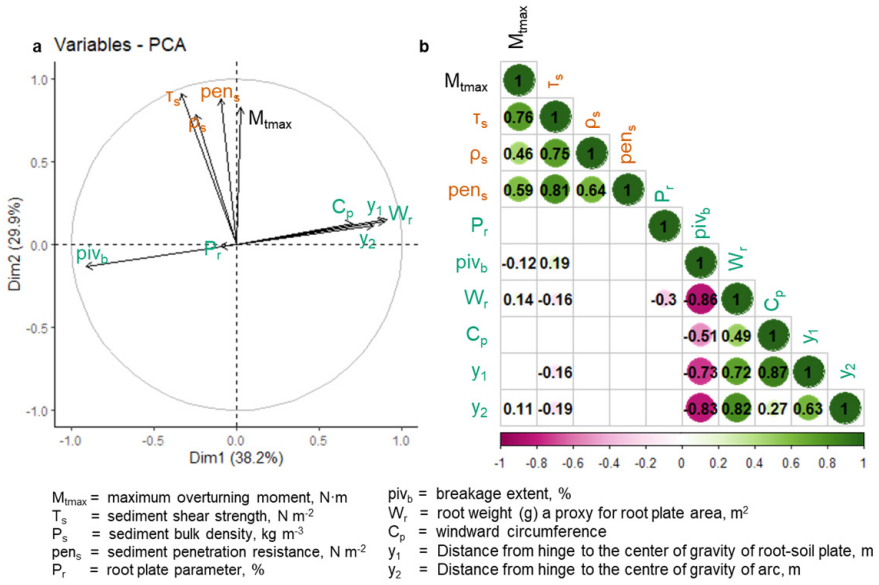

Figure A3. (**a**) Correlation circle showing correlation between variables and Principal Components and (**b**) all significant ($\alpha = 0.05$) correlations between variables where darker greens represent a larger positive correlation, and darker pinks represent a negative correlation. Symbol colors indicate sediment (brown) and mimic (green)-related properties.

When fitting the average linear model ($y = -0.07 + 0.23x$) for each root mass distribution, we found significant differences in the residuals between the root mass distributions (Figures 7 and A4), showing that the root mass distribution influenced stability.

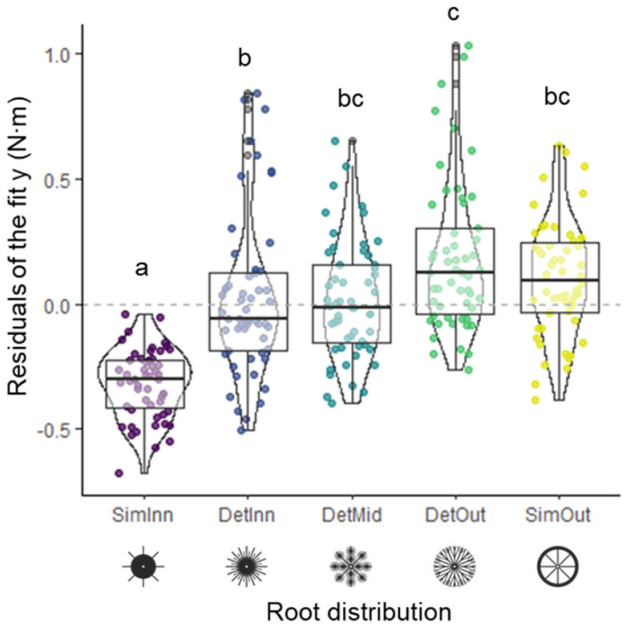

Figure A4. Residuals (jitterplot with boxplot and violinplot) of the linear regressions from Figure 7, showing the residuals of different root plates in different colours. Significance letters (a, b, bc, c) ($\alpha = 0.05$) from Dunn's test. Breakages were half (25% of the complete plate) or complete (45%) breakage at the windward, leeward, or both sides of the root plate (see Figure 2b).

References

1. Gijsman, R.; Horstman, E.M.; van der Wal, D.; Friess, D.A.; Swales, A.; Wijnberg, K.M. Nature-Based Engineering: A Review on Reducing Coastal Flood Risk With Mangroves. *Front. Mar. Sci.* **2021**, *8*, 702412. [CrossRef]
2. van Hespen, R.; Hu, Z.; Borsje, B.; De Dominicis, M.; Friess, D.A.; Jevrejeva, S.; Kleinhans, M.G.; Maza, M.; van Bijsterveldt, C.E.; Van der Stocken, T.; et al. Mangrove forests as a nature-based solution for coastal flood protection: Biophysical and ecological considerations. *Water Sci. Eng.* **2023**, *16*, 1–13. [CrossRef]
3. Mazda, Y.; Magi, M.; Ikeda, Y.; Kurokawa, T.; Asano, T. Wave reduction in a mangrove forest dominated by Sonneratia sp. *Wetl. Ecol. Manag.* **2006**, *14*, 365–378. [CrossRef]
4. Quartel, S.; Kroon, A.; Augustinus, P.G.E.F.; Van Santen, P.; Tri, N.H. Wave attenuation in coastal mangroves in the Red River Delta, Vietnam. *J. Asian Earth Sci.* **2007**, *29*, 576–584. [CrossRef]
5. Horstman, E.M.; Dohmen-Janssen, C.M.; Narra, P.M.F.; van den Berg, N.J.F.; Siemerink, M.; Hulscher, S.J.M.H. Wave attenuation in mangroves: A quantitative approach to field observations. *Coast. Eng.* **2014**, *94*, 47–62. [CrossRef]
6. Kobashi, D.; Mazda, Y. Tidal Flow in Riverine-Type Mangroves. *Wetl. Ecol. Manag.* **2005**, *13*, 615–619. [CrossRef]
7. Sánchez-Núñez, D.A.; Bernal, G.; Pineda, J.E.M. The Relative Role of Mangroves on Wave Erosion Mitigation and Sediment Properties. *Estuaries Coasts* **2019**, *42*, 2124–2138. [CrossRef]
8. Saintilan, N.; Khan, N.S.; Ashe, E.; Kelleway, J.J.; Rogers, K.; Woodroffe, C.D.; Horton, B.P. Thresholds of Mangrove Survival Under Rapid Sea Level Rise. 2020. Available online: http://science.sciencemag.org/ (accessed on 3 March 2024).
9. Krauss, K.W.; Osland, M.J. Tropical cyclones and the organization of mangrove forests: A review. *Ann. Bot.* **2020**, *125*, 213–234. [CrossRef] [PubMed]
10. van Bijsterveldt, C.E.J.; Herman, P.M.J.; van Wesenbeeck, B.K.; Ramadhani, S.; Heuts, T.S.; van Starrenburg, C.; Tas, S.A.J.; Triyanti, A.; Helmi, M.; Tonneijck, F.H.; et al. Subsidence reveals potential impacts of future sea level rise on inhabited mangrove coasts. *Nat. Sustain.* **2023**, *6*, 1565–1577. [CrossRef]
11. Alongi, D.M. Carbon sequestration in mangrove forests. *Carbon. Manag.* **2012**, *3*, 313–322. [CrossRef]
12. Primavera, J.H. Mangroves as Nurseries: Shrimp Populations in Mangrove and Non-mangrove Habitats. *Estuar. Coast. Shelf Sci.* **1998**, *46*, 457–464. [CrossRef]
13. Palacios, M.L.; Cantera, J.R. Mangrove timber use as an ecosystem service in the Colombian Pacific. *Hydrobiologia* **2017**, *803*, 345–358. [CrossRef]
14. Smith, T.J., III; Boto, K.G.; Frusher, S.D.; Giddins, R.L. Keystone Species and Mangrove Forest Dynamics: The Influence of Burrowing by Crabs on Soil Nutrient Status and Forest Productivity. *Estuar. Coast. Shelf Sci.* **1991**, *33*, 419–432. [CrossRef]
15. Cahoon, D.R.; Hensel, P.; Rybczyk, J.M.; Perez, B.C.; Christopher, B. *Hurricane Mitch: Impacts on Mangrove Sediment Elevation Dynamics and Long-Term Mangrove Sustainability Recommended Citation*; Western Washington University: Bellingham, WA, USA, 2002.
16. Jiménez, J.A.; Lugo, A.E.; Cintrón, G. Tree Mortality in Mangrove Forests. *Biotropica* **1985**, *17*, 177–185. [CrossRef]
17. Mo, Y.; Simard, M.; Hall, J.W. Tropical cyclone risk to global mangrove ecosystems: Potential future regional shifts. *Front. Ecol. Environ.* **2023**, *21*, 269–274. [CrossRef]
18. Anthony, E.J.; Gardel, A.; Gratiot, N.; Proisy, C.; Allison, M.A.; Dolique, F.; Fromard, F. The Amazon-influenced muddy coast of South America: A review of mud-bank–shoreline interactions. *Earth Sci. Rev.* **2010**, *103*, 99–121. [CrossRef]
19. Ellison, J.C. Impacts of Sediment Burial on Mangroves. *Mar. Pollut. Bull.* **1999**, *37*, 420–426. [CrossRef]
20. Urata, T.; Shibuya, M.; Koizumi, A.; Torita, H.; Cha, J. Both stem and crown mass affect tree resistance to uprooting. *J. For. Res.* **2012**, *17*, 65–71. [CrossRef]
21. Sagi, P.; Newson, T.; Miller, C.; Mitchell, S. Stem and root system response of a Norway spruce tree (*Picea abies* L.) under static loading. *For. Int. J. For. Res.* **2019**, *92*, 460–472. [CrossRef]
22. Achim, A.; Nicoll, B.C. Modelling the anchorage of shallow-rooted trees. *For. Int. J. For. Res.* **2009**, *82*, 273–284. [CrossRef]
23. COUTTS, M.P. Components of Tree Stability in Sitka Spruce on Peaty Gley Soil. *For. Int. J. For. Res.* **1986**, *59*, 173–197. [CrossRef]
24. Fourcaud, T.; Ji, J.-N.; Zhang, Z.-Q.; Stokes, A. Understanding the Impact of Root Morphology on Overturning Mechanisms: A Modelling Approach. *Ann. Bot.* **2008**, *101*, 1267–1280. [CrossRef] [PubMed]
25. Ow, L.F.; Harnas, F.R.; Indrawan, I.G.B.; Sahadewa, A.; Sim, E.K.; Rahardjo, H.; Leong, E.C.; Fong, Y.K.; Tan, P.Y. Tree-pulling experiment: An analysis into the mechanical stability of rain trees. *Trees* **2010**, *24*, 1007–1015. [CrossRef]
26. Ferreira, T.O.; Otero, X.L.; de Souza Junior, V.S.; Vidal-Torrado, P.; Macías, F.; Firme, L.P. Spatial patterns of soil attributes and components in a mangrove system in Southeast Brazil (São Paulo). *J. Soils Sediments* **2010**, *10*, 995–1006. [CrossRef]
27. Soares, M.L.G.; Schaeffer-Novelli, Y. Above-ground biomass of mangrove species. I. Analysis of models. *Estuar. Coast. Shelf Sci.* **2005**, *65*, 1–18. [CrossRef]
28. Gilman, E.L.; Ellison, J.; Duke, N.C.; Field, C. Threats to mangroves from climate change and adaptation options: A review. *Aquat. Bot.* **2008**, *89*, 237–250. [CrossRef]

29. Winterwerp, J.C.; Albers, T.; Anthony, E.J.; Friess, D.A.; Mancheño, A.G.; Moseley, K.; Muhari, A.; Naipal, S.; Noordermeer, J.; Oost, A.; et al. Managing erosion of mangrove-mud coasts with permeable dams—Lessons learned. *Ecol. Eng.* **2020**, *158*, 106078. [CrossRef]
30. Van Loon, A.F.; Brake, B.T.; Van Huijgevoort, M.H.J.; Dijksma, R. Hydrological classification, a practical tool for mangrove restoration. *PLoS ONE* **2016**, *11*, 3. [CrossRef]
31. Watson, J.G. *Mangrove Forests of the Malay Peninsula*; Printed by Fraser & Neave: Singapore, 1928; Available online: https://www.biodiversitylibrary.org/item/331433 (accessed on 10 November 2024).
32. PLASTIM. *Product Data Sheet Nylon 12*; PLASTIM: Gloucester, UK, 2015.
33. Njana, M.A.; Bollandsås, O.M.; Eid, T.; Zahabu, E.; Malimbwi, R.E. Above- and belowground tree biomass models for three mangrove species in Tanzania: A nonlinear mixed effects modelling approach. *Ann. For. Sci.* **2016**, *73*, 353–369. [CrossRef]
34. Njana, M.A.; Eid, T.; Zahabu, E.; Malimbwi, R. Procedures for quantification of belowground biomass of three mangrove tree species. *Wetl. Ecol. Manag.* **2015**, *23*, 749–764. [CrossRef]
35. Johnson, J.B.; Omland, K.S. Model selection in ecology and evolution. *Trends Ecol. Evol.* **2004**, *19*, 101–108. [CrossRef]
36. Zanetti, C.; Vennetier, M.; Mériaux, P.; Provansal, M. Plasticity of tree root system structure in contrasting soil materials and environmental conditions. *Plant Soil.* **2015**, *387*, 21–35. [CrossRef]
37. Hill, J.W.; Bennion, V.; Lovelock, C.E. Mangrove tree strength estimated with field experiments. *Ecol. Eng.* **2024**, *203*, 107259. [CrossRef]
38. Vovides, A.G.; Berger, U.; Grueters, U.; Guevara, R.; Pommerening, A.; Lara-Domínguez, A.L.; López-Portillo, J. Change in drivers of mangrove crown displacement along a salinity stress gradient. *Funct. Ecol.* **2018**, *32*, 2753–2765. [CrossRef]
39. Vovides, A.G.; Berger, U.; Balke, T. Chapter 5—Morphological plasticity and survival thresholds of mangrove plants growing in active sedimentary environments. In *Dynamic Sedimentary Environments of Mangrove Coasts*; Sidik, F., Friess, D.A., Eds.; Elsevier: Amsterdam, The Netherlands, 2021; pp. 121–140. [CrossRef]
40. Nicoll, B.C.; Ray, D. Adaptive growth of tree root systems in response to wind action and site conditions. *Tree Physiol.* **1996**, *16*, 891–898. [CrossRef]
41. McKee, K.L. Interspecific Variation in Growth, Biomass Partitioning, and Defensive Characteristics of Neotropical Mangrove Seedlings: Response to Light and Nutrient Availability. *Am. J. Bot.* **1995**, *82*, 299–307. [CrossRef]
42. Ye, Y.; Tam, N.F.Y.; Wong, Y.S.; Lu, C.Y. Growth and physiological responses of two mangrove species (Bruguiera gymnorrhiza and Kandelia candel) to waterlogging. *Environ. Exp. Bot.* **2003**, *49*, 209–221. [CrossRef]
43. Nicoll, B.C.; Gardiner, B.A.; Rayner, B.; Peace, A.J. Anchorage of coniferous trees in relation to species, soil type, and rooting depth. *Can. J. For. Res.* **2006**, *36*, 1871–1883. [CrossRef]
44. Rahardjo, H.; Harnas, F.R.; Leong, E.C.; Tan, P.Y.; Fong, Y.K.; Sim, E.K. Tree stability in an improved soil to withstand wind loading. *Urban. For. Urban. Green.* **2009**, *8*, 237–247. [CrossRef]
45. Gillen, M.N.; Messerschmidt, T.C.; Kirwan, M.L. Biophysical controls of marsh soil shear strength along an estuarine salinity gradient. *Earth Surf. Dynam.* **2021**, *9*, 413–421. [CrossRef]
46. Grabowski, R.C.; Droppo, I.G.; Wharton, G. Erodibility of cohesive sediment: The importance of sediment properties. *Earth Sci. Rev.* **2011**, *105*, 101–120. [CrossRef]
47. Yoshikai, M.; Nakamura, T.; Suwa, R.; Argamosa, R.; Okamoto, T.; Rollon, R.; Basina, R.; Primavera-Tirol, Y.H.; Blanco, A.C.; Adi, N.S.; et al. Scaling relations and substrate conditions controlling the complexity of Rhizophora prop root system. *Estuar. Coast. Shelf Sci.* **2021**, *248*, 107014. [CrossRef]
48. Mendez, F.J.; Losada, I.J. An empirical model to estimate the propagation of random breaking and nonbreaking waves over vegetation fields. *Coast. Eng.* **2004**, *51*, 103–118. [CrossRef]
49. Morison, J.R.; Johnson, J.W.; Schaaf, S.A. The Force Exerted by Surface Waves on Piles. *J. Pet. Technol.* **1950**, *2*, 149–154. [CrossRef]
50. Banerjee, K.; Bal, G.; Mitra, A. How Soil Texture Affects the Organic Carbon Load in the Mangrove Ecosystem? A Case Study from Bhitarkanika, Odisha. In *Environmental Pollution, Water Science and Technology Library*; Singh, V.P., Yadav, S., Yadava, R.N., Eds.; Springer Singapore: Singapore, 2018; pp. 329–341. [CrossRef]
51. Bulmer, R.H.; Lundquist, C.J.; Schwendenmann, L. Sediment properties and CO_2 efflux from intact and cleared temperate mangrove forests. *Biogeosciences* **2015**, *12*, 6169–6180. [CrossRef]
52. Dewiyanti, I.; Darmawi, D.; Muchlisin, Z.A.; Helmi, T.Z.; Imelda, I.; Defira, C.N. Physical and chemical characteristics of soil in mangrove ecosystem based on differences habitat in Banda Aceh and Aceh Besar. *IOP Conf. Ser. Earth Environ. Sci.* **2021**, *674*, 012092. [CrossRef]
53. Duan, J.; Han, J.; Zhou, H.; Lau, Y.L.; An, W.; Wei, P.; Cheung, S.G.; Yang, Y.; Tam, N.F. Development of a digestion method for determining microplastic pollution in vegetal-rich clayey mangrove sediments. *Sci. Total Environ.* **2020**, *707*, 136030. [CrossRef]
54. Stokes, D.J.; Harris, R.J. Sediment properties and surface erodibility following a large-scale mangrove (Avicennia marina) removal. *Cont. Shelf Res.* **2015**, *107*, 1–10. [CrossRef]

55. Takagi, H.; Xiong, Y.; Furukawa, F. Track analysis and storm surge investigation of 2017 Typhoon Hato: Were the warning signals issued in Macau and Hong Kong timed appropriately? *Georisk Assess. Manag. Risk Eng. Syst. Geohazards* **2018**, *12*, 297–307. [CrossRef]
56. van Hespen, R.; Hu, Z.; Peng, Y.; Borsje, B.W.; Kleinhans, M.; Ysebaert, T.; Bouma, T.J. Analysis of coastal storm damage resistance in successional mangrove species. *Limnol Ocean.* **2021**, *66*, 3221–3236. [CrossRef]